



In situ estimates of submesoscale horizontal eddy diffusivity across an ocean front

Francesco Nencioli, Francesco d'Ovidio, Andrea M. Doglioli, Anne Petrenko

► To cite this version:

Francesco Nencioli, Francesco d'Ovidio, Andrea M. Doglioli, Anne Petrenko. In situ estimates of submesoscale horizontal eddy diffusivity across an ocean front. *Journal of Geophysical Research. Oceans*, 2013, 118 (12), pp.7066-7080. 10.1002/2013JC009252 . hal-00934857

HAL Id: hal-00934857

<https://hal.science/hal-00934857>

Submitted on 3 Jan 2022

HAL is a multi-disciplinary open access archive for the deposit and dissemination of scientific research documents, whether they are published or not. The documents may come from teaching and research institutions in France or abroad, or from public or private research centers.

L'archive ouverte pluridisciplinaire **HAL**, est destinée au dépôt et à la diffusion de documents scientifiques de niveau recherche, publiés ou non, émanant des établissements d'enseignement et de recherche français ou étrangers, des laboratoires publics ou privés.

Copyright

In situ estimates of submesoscale horizontal eddy diffusivity across an ocean front

F. Nencioli,^{1,2} F. d'Ovidio,^{3,4} A. M. Doglioli,^{1,2} and A. A. Petrenko^{1,2}

Received 3 July 2013; revised 18 October 2013; accepted 2 December 2013; published 20 December 2013.

[1] In the last decade, the rapid advancements in computational power have favored the development of high-resolution numerical models capable of directly resolving small-scale structures such as fronts and filaments. Such models have greatly improved our understanding of submesoscale dynamics. At the same time, the small dimensions and short duration of these structures still pose major challenges for small-scale dedicated field experiments. For this reason, submesoscale studies from in situ observations are still relatively scarce and quantitative estimates of key physical parameters for high-resolution numerical models, such as horizontal eddy diffusivity, are still lacking. This study presents a novel approach for computing in situ horizontal eddy diffusivity associated with frontal structures by combining cross-front widths derived from surface thermosalinograph sections with stirring rates estimated from Lagrangian drifter trajectories. The method is applied to the measurements collected across a frontal structure observed in the western part of the Gulf of Lion during the Latex10 campaign (Lagrangian Transport EXperiment, 1–24 September 2010). A total of 76 estimates of eddy diffusivity were obtained for strain rates of 0.70 and 1.21 day^{−1} and front widths (horizontal scales) ranging between 1 and 4 km. The estimates are log-normally distributed, with 70% of the values ranging between 0.4 and 5 m² s^{−1}. Further analysis based on high-resolution simulations and remote sensed observations, as well as dedicated field experiments will help to assess the robustness of some of the assumptions at the base of the proposed approach, and to extend the results to different ocean regions.

Citation: Nencioli, F., F. d'Ovidio, A. M. Doglioli, and A. A. Petrenko (2013), In situ estimates of submesoscale horizontal eddy diffusivity across an ocean front, *J. Geophys. Res. Oceans*, 118, 7066–7080, doi:10.1002/2013JC009252.

1. Introduction

[2] Oceanic submesoscale is characterized by scales of motion smaller than the Rossby radius of deformation, but large enough to be influenced by Earth's rotation and density stratification [see Thomas *et al.*, 2008, for a review]. Typical submesoscale structures include fronts, eddies, and filaments with spatial scales of $\mathcal{O}(1\text{--}10)\text{km}$, and time scales of $\mathcal{O}(1)\text{day}$. A first indication of the ubiquity of these structures at both mid and high-latitudes came

from satellite imagery of surface tracers (i.e., sea surface temperature and ocean color), for long characterized by resolutions ($\mathcal{O}(1)\text{ km}$ or less) capable of resolving the submesoscale (e.g., pioneer studies by Gower *et al.* [1980] and Millot [1982]). However, exhaustive analysis of oceanic submesoscale dynamics has been possible only after the recent advancements in computational power and the improvements in physical and planktonic ecosystem models. In the last decade, these have favored the development of several studies based on high-resolution numerical simulations which focused on the investigation of submesoscale processes. Such studies have significantly improved our understanding of the contribution of submesoscale dynamics to the ocean energy budget [e.g., Capet *et al.*, 2008a; Molemaker *et al.*, 2010], mixed layer dynamics [e.g., Fox Kemper *et al.*, 2008; Boccaletti *et al.*, 2007], as well as primary production and biogeochemical cycles [e.g., Lévy *et al.*, 2001; Calil and Richards, 2010; Perruche *et al.*, 2011; Mahadevan *et al.*, 2012; Lévy *et al.*, 2012].

[3] The models used to investigate submesoscale dynamics can be broadly divided into two main categories: (i) submesoscale resolving models—characterized by domains of $\mathcal{O}(100\text{--}1000)\text{km}$ and by horizontal resolutions of $\mathcal{O}(0.1\text{--}1)\text{km}$, capable of representing the mesoscale-driven submesoscale dynamics at the basin scale [e.g., Capet *et al.*,

Additional supporting information may be found in the online version of this article.

¹Aix-Marseille Université, CNRS/INSU, IRD, MIO, UM 110, 13288, Marseille, France.

²Université de Toulon, CNRS/INSU, IRD, MIO, UM 110, La Garde, France.

³Sorbonne Universités, UPMC Univ Paris 06, UMR 7159, LOCEAN-IPSL, Paris, France.

⁴CNRS, UMR 7159, LOCEAN-IPSL, Paris, France.

Corresponding author: F. Nencioli, Mediterranean Institute of Oceanography, Aix-Marseille University, Campus de Luminy, Case 901, FR-13288 Marseille CEDEX 09, France. (francesco.nencioli@univ-amu.fr)

©2013. American Geophysical Union. All Rights Reserved.
2169-9275/13/10.1002/2013JC009252

2008b; Klein *et al.*, 2008]; (ii) large eddy simulation (LES) models—characterized by domains of $\mathcal{O}(1-10)$ km and horizontal resolutions down to $\mathcal{O}(1)$ m, more local and thus capable of resolving the three-dimensional turbulent motions responsible for the forward cascade of energy [e.g., Taylor and Ferrari, 2010; Özgökmen *et al.*, 2011]. Both categories of models require turbulent closure schemes in order to parametrize the viscous and diffusive effects associated with unresolved subgrid processes. The simplest closure schemes usually assume constant horizontal eddy viscosities and diffusivities, whereas more complex schemes are based on spatio-temporally varying ones which depend on the dynamical characteristics of the resolved scales of motion [e.g., Smagorinsky, 1963; James, 1996; Le Sommer *et al.*, 2011]. Closure schemes of this type are also implemented in another category of models, the so-called mesoscale ocean large-eddy simulation models (MOLES) [Fox Kemper and Menemenlis, 2008]. These are novel ocean general circulation models capable of partly resolving the mesoscale, and thus particularly relevant for global ocean and climate studies.

[4] The accurate tuning of the values of eddy viscosity and diffusivity represents a key aspect for any closure scheme, since the two parameters control the rate of energy dissipation (eddy viscosity) and the dispersion of physical and biogeochemical tracers (eddy diffusivity) [Bracco *et al.*, 2009] in the model. Although it is well established that their values scale with the grid resolution [Okubo, 1971], recent studies have shown that high-resolution models can remain numerically stable over a broad range of eddy viscosities and diffusivities, and that their results are highly sensitive to them [Lévy *et al.*, 2012].

[5] In LES, while the dominant reason of success is due to resolving all the relevant turbulent coherent structures in a given problem, avoiding the use of excessive viscosity also plays a role (albeit secondary). Realistic values for eddy viscosity and diffusivity can be tuned by comparison with direct numerical simulations (DNS) [Özgökmen *et al.*, 2009]. In fact, through the Kolmogorov's universal scaling at the inertial-subscale range, the level of dissipation estimated from DNS can be assumed to be appropriate also for LES subgrid processes. This approach cannot be applied for submesoscale resolving simulations, since the small domains characteristic of DNS lack the mesoscale-induced straining of the density field which is a fundamental contributor for the development of submesoscale dynamics [e.g., Capet *et al.*, 2008b]. For this reason, recent studies have started to systematically investigate the performance of high-resolution simulations in representing submesoscale dynamics for different levels of dissipation, both physical (due to different closure approaches) [Ramachandran *et al.*, 2013], as well as numerical [Marchesiello *et al.*, 2011]. Due to the lack of existing guidelines from direct measurements, these studies have defined the optimal levels of dissipation based mainly on the analysis of eddy kinetic energy budgets.

[6] The present study aims at filling this gap by providing in situ estimates of horizontal eddy diffusivity across an ocean front. As already mentioned, such eddy diffusivity represents an approximation of horizontal eddy transport parametrized as a diffusivity. As such, it is only appropriate when there is a scale separation between the resolved and

unresolved physics, i.e., when the processes generating the front are resolved, but not its instabilities. For this reason, our estimates could be directly used as a model parametrization when submesoscale processes are not resolved (e.g., MOLES regime or coarser). At the same time, they could also be used as benchmarks for sensitivity analysis of higher-resolution models capable of resolving the processes responsible for the observed eddy diffusivities (i.e., submesoscale-permitting and finer models).

[7] In the last two decades, in situ estimates of horizontal eddy diffusivity in the oceans have been mainly computed from three different platforms: Lagrangian drifters, satellite observations and passive-tracer experiments. Lagrangian methods allow the quantification of eddy diffusivity either from the statistical analysis of single and multiple particle trajectories [see LaCasce, 2008, for an overview], or from inverse Lagrangian stochastic models (LSM) [e.g., Griffa *et al.*, 1995]. Due to technological (e.g., low frequency of acquisition of drifter position), methodological (e.g., diffusivity values estimated by averaging over large areas due to sparse drifter data), and experimental design limitations (e.g., drifter deployments mainly focused to the investigation of large-scale circulation), these methods have so far allowed to retrieve values of eddy diffusivities only at the mesoscale. Typical values are of $\mathcal{O}(1000)\text{m}^2\text{s}^{-1}$ for spatial scales of $\mathcal{O}(100)\text{km}$ [e.g., Lumpkin *et al.*, 2002; Zhurbas and Oh, 2004; Sallée *et al.*, 2008; Lumpkin and Elipot, 2010; Rypina *et al.*, 2012]. In the last years, advancements in drifter technology, combined with the development of high-frequency radar networks for monitoring coastal circulation at high spatial and temporal resolution, have favored the development of Lagrangian studies specifically designed to investigate coastal dynamics at the submesoscale [e.g., Haza *et al.*, 2010; Ohlmann *et al.*, 2012; Schroeder *et al.*, 2012]. Although such studies have helped improving our understanding of the contribution of local and nonlocal processes in regulating relative dispersions at scales below the Rossby radius of deformation, to our knowledge they have not yet provided a quantification of eddy diffusivity at the submesoscale.

[8] Eddy diffusivities from satellite observations are usually based on a passive-tracer approach: first, the advection of a passive tracer is simulated using altimetry derived velocity fields; then different diagnostics are applied to the resulting tracer distribution to retrieve the values of eddy diffusivity. The “effective diffusivity” method [Nakamura, 1996], based on the rate of material transport across tracer contours, is most commonly applied [e.g., Marshall *et al.*, 2006; Shuckburgh *et al.*, 2009; Abernathey and Marshall, 2013]. This method has been found to be particularly effective in regions like the Southern Ocean, characterized by a monotonic latitudinal gradient and a mean flow perpendicular to it. Other methods, such as the Osborn-Cox diffusivity [Nakamura, 2001], based on the tracer variance budget, have been recently applied to extend the analysis to other regions of the ocean [Abernathey and Marshall, 2013]. Due to the resolution of altimetry velocity fields (e.g., AVISO global velocities are available at $1/3^\circ$), and the time scales required for the advection of the tracer of $\mathcal{O}(\text{months})$, these estimates of eddy diffusivity are associated with the large-scale dynamics, and thus are analogous to the ones obtained from Lagrangian methods [Klocker *et al.*, 2012].

[9] More relevant to the results of the present study are the eddy diffusivities at smaller scales obtained from in situ passive-tracer experiments, such as NATRE [e.g., *Ledwell et al.*, 1998; *Stanton et al.*, 1998; *Abraham et al.*, 2000; *Martin et al.*, 2001]. Such estimates are based on the hypothesis that, due to the local mesoscale stirring (approximately two-dimensional and divergence-free) the initial shape of a tracer patch will elongate along one direction while thinning along the other. The width of the patch will keep decreasing until the effect of mesoscale stirring is balanced by smaller scale diffusion. Thus, eddy diffusivity can be computed by combining estimates of the strain rate (either from successive in situ mapping, as in *Ledwell et al.* [1998], or from the analysis of satellite imagery of surface chlorophyll, as in *Abraham et al.* [2000]), with in situ measurements of the patch width. Eddy diffusivities computed using this approach range from 0.5 to 25 m² s⁻¹ for tracer filaments with widths between 1 and 10 km. These estimates remain the only few available at those scales from in situ observations. For this reason, they still represent an important guideline for high-resolution numerical models, as well as the closest term of comparison for this study.

[10] In this study, we present a method to estimate in situ eddy diffusion coefficients at the submesoscale based on the same hypothesis of balance between mesoscale straining and small-scale mixing adopted for passive-tracer experiments. However, instead of using the width of a tracer patch, our analysis will be based on the width of a thermohaline front. This approach is analogous to the one adopted by *Flament et al.* [1985], who provided an estimate of eddy diffusivity by combining the cross front width derived from temperature variations observed along a single ship-based cross-front section, with an approximate estimate of the cross-front convergence rate derived from successive satellite imagery of surface temperature. Here instead, we will first obtain a series of estimates of the front width by fitting a series of high-resolution temperature, as well as salinity cross-front sections from the ship-mounted thermosalinograph with an analytical model for the cross-front profile at the equilibrium. The front widths will be then combined with concomitant estimates of the average local strain rate derived from the dispersion of two arrays of Lagrangian drifters to retrieve horizontal eddy diffusivities. A similar strategy based on combining reconstructed tracer profiles and Lagrangian diagnostics was also developed for estimating diffusivity in the troposphere by *Legras et al.* [2005] and *Pisso et al.* [2009]. In our case, thanks to the easier accessibility of the ocean surface compared to the troposphere, the local cross-front profiles are measured in situ and then modeled analytically. Our approach allowed the computation of multiple estimates of eddy diffusion coefficients, which are used to test the robustness of the method, and to obtain statistically significant estimates.

2. Data and Methods

2.1. Observations From the Latex10 campaign

[11] The data used in this study were collected during the Latex10 campaign (1–24 September 2010) in the western Gulf of Lion (hereafter GoL; Figure 1, top) aboard the *R/V Le Téthys II*. This was the third and last field experi-

ment of the LAgrangian Transport EXperiment (LATEX, 2008–2011), which focused on the investigation of (sub)-mesoscale dynamics and cross-shelf exchanges in the region [*Hu et al.*, 2009, 2011a, 2011b; *Campbell et al.*, 2012; *Kersalé et al.*, 2013]. During Latex10, an adaptive sampling strategy, which combined satellite altimetry, ship-based Acoustic Current Doppler Profiler (ADCP) measurements, and iterative Lagrangian drifter releases, allowed to identify and track in situ attractive and repelling Lagrangian coherent structures (LCS) for a period of 12 days (Figure 1, bottom left) [*Nencioli et al.*, 2011].

[12] Analysis of AVHRR (Advanced Very High Resolution Radiometer) channel 4 imagery (provided by Météo-France) revealed that the detected LCSs were associated with a strong thermal front. AVHRR channel 4 measurements are usually inaccurate in estimating the absolute values of the sea surface temperature (SST). However, AVHRR channel 4 (hereafter pseudo-SST) imagery has shown to accurately identify the spatial distribution of SST gradients, as also confirmed by comparisons with the thermosalinograph data (see supporting information). This, along with the higher spatial (1 km) and temporal resolution (up to four images per day in the western part of the GoL), makes pseudo-SST imagery particularly suited for a qualitative analysis of the distribution, as well as the temporal evolution, of small-scale structures associated with strong SST gradients such as the Latex10 front (Figure 1, bottom right). This was also evidenced during previous LATEX campaigns when pseudo-SST images were used to investigate the dynamics of local anticyclonic eddies [e.g., *Hu et al.*, 2011a; *Kersalé et al.*, 2013].

[13] During the Latex10 campaign, in situ surface temperature and salinity (hereafter SST and SSS, respectively) were measured by a hull-mounted SeaBird SBE21 thermosalinograph at a depth of 2 m. The observations were recorded at a frequency of 4 Hz, with an accuracy of 0.01°C for the temperature and 0.005 psu for the salinity. Given a cruise speed of eight knots, this sampling frequency allowed to collect cross-front sections with an along-track spatial resolution of about 60 m. Measurements of SST and SSS were recorded continuously along the ship track from 7 to 24 September except during profiling operations, when the thermosalinograph was turned off. No measurements were collected on 13, 16, and 19 September due to strong wind conditions.

[14] The campaign design also included Slocum glider observations to retrieve temperature and salinity sections across the front. Unfortunately, the glider was lost at sea on 18 September and never recovered. Because of that, information on the structure of the water column across the front is only limited to the low-resolution temperature data remotely transmitted by the glider while at the surface between dives, and to the 34 SeaBird SBE 19 CTD profiles sparsely collected from 11 to 23 September (see supporting information). While such observations provide a good indication of the depth of the upper mixed layer in the region, they do not allow an accurate characterization of the vertical structure of the front. For this reason, our analysis focuses entirely on its surface characteristics.

[15] Estimates of the average local strain rate are based on the trajectories of 14 Technocean Surface Velocity Program (SVP) subsurface drifters. Each drifter was tethered

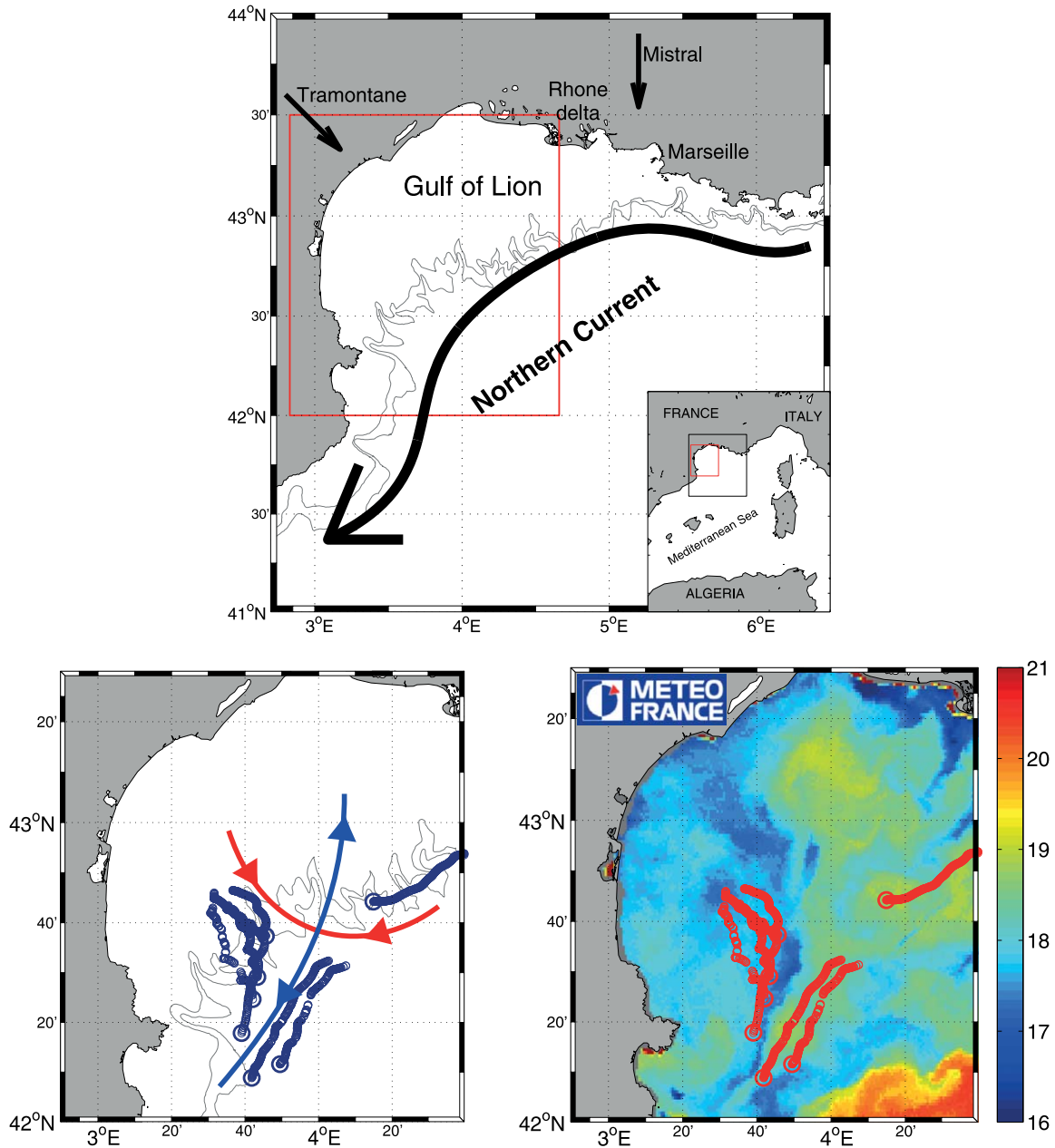


Figure 1. (top) Bathymetry of the Gulf of Lion (200 and 500 m isobaths). Black arrows indicate the Northern Current, and the Tramontane and Mistral winds. The red rectangle indicates the region of focus of the Latex10 campaign. (bottom) Drifter trajectories from 12 to 14 September. Larger circles indicate the final position of the drifters on 14 September. In red and blue are the reconstructed repelling and attracting LCSs, respectively. The intersection between repelling and attracting LCSs marks the location of the hyperbolic point. (bottom right) Same drifter trajectories as in the left plot superimposed to AVHRR pseudo-SST (shaded) for 15 September, evidencing the front between colder continental-shelf waters and warmer open NW Mediterranean waters (from *Nencioli et al.* [2011]).

to a holey-sock drogue centered at 15 m depth, and equipped with a GPS transmitter which communicated its position every 30 min. The drifters were deployed in arrays of varying number, with initial separation distances between the drifters ranging from 3 to 5 km. Of the three array deployments performed during Latex10 [see *Nencioli et al.*, 2011, for more details], only the first two (hereafter

Lyap01, launched on 12 September, and Lyap02, launched on 18 September) will be analyzed in this study. In addition to those, four additional drifters with a drogue centered at 50 m were deployed in the eastern GoL at the beginning of the campaign. These were used exclusively to track the circulation along the GoL continental slope, and were not included in the computation of the strain rate.

2.2. Analytical Solution for Cross-Front Profiles

[16] Our analysis is based on an analytical expression for the cross-front profiles of SST and SSS obtained by solving a simplified version of the one-dimensional advection-diffusion equation. In section 3.1, we will show that the assumptions which allow to simplify such equation are consistent with the dynamical characteristics of the frontal structure detected during Latex10.

[17] Given a tracer T , and assuming that (i) horizontal motions are larger than vertical ones, (ii) source and sinks (i.e., exchanges with the atmosphere) are negligible, and (iii) cross-front gradients are larger than along-front ones, the tracer advection-diffusion equation along the cross-front direction x is given by

$$\frac{\partial T}{\partial t} + u \frac{\partial T}{\partial x} = K_H \frac{\partial^2 T}{\partial x^2} \quad (1)$$

where u is the velocity component along the cross-front direction, and K_H the cross-frontal horizontal eddy diffusivity, assumed to be constant along the cross-frontal direction.

[18] *Nencioli et al.* [2011] showed that the Latex10 front coincided with an attractive LCS associated with a slowly moving hyperbolic point (Figure 1). The cross-front velocity component u can be therefore assumed to be function of the convergence rate toward the attractive LCS. Specifically, u can be expressed as the product between the strain rate γ and the distance from the LCS/front axis ($x - x_0$), with x_0 the front axis position along the transect. If we also assume the front to be at the equilibrium (this hypothesis will be tested and discussed in section 3.5), equation (1) can be further simplified to

$$-\gamma(x - x_0) \frac{dT}{dx} = K_H \frac{d^2 T}{dx^2} \quad (2)$$

which is the ordinary differential equation describing the cross-front variation of T .

[19] An analytical solution to equation (2) can be found in terms of the error function [see also *Thorpe*, 1983; *Ledwell et al.*, 1998; *Abraham et al.*, 2000]. By imposing the boundary conditions away from the front axis $T_{x \rightarrow -\infty} = T_1$ and $T_{x \rightarrow \infty} = T_2$, the resulting solution for the tracer profile $T(x)$ is

$$T(x) = C_1 + C_2 \operatorname{erf}(C_3(x - C_4)) \quad (3)$$

with

$$C_1 = \frac{T_2 + T_1}{2}; \quad C_2 = \frac{T_2 - T_1}{2}; \quad C_3 = \frac{1}{\sqrt{2}} \sqrt{\frac{\gamma}{K_H}}; \quad C_4 = x_0 \quad (4)$$

[20] The values of these coefficients are all dependent on measurable physical quantities. The four coefficients modify the shape of the error function, determining the characteristics of a specific T profile: C_1 and C_4 determine the translation of the error function along the y and x axes, respectively; C_2 and C_3 determine the stretching of the error function along the y and x axes, respectively. C_3 is therefore the sole parameter controlling the width of the T front. Its value depends entirely on the ratio between the

strain rate γ and the eddy diffusivity K_H , and not on the tracer values T_1 and T_2 at the two extremes of the front. Thus, large-scale advection and small-scale mixing are the only two processes affecting the width of the front at the equilibrium. In particular, large-scale advection tends to steepen the front (the larger γ , the larger C_3 , the narrower the resulting error function), while small-scale mixing tends to flatten it (the larger K_H , the smaller C_3 , the broader the resulting error function).

[21] By inverting the relation for the C_3 coefficient in equation (4), we can obtain an expression for K_H as a function of C_3 and γ

$$K_H = \frac{\gamma}{2C_3^2} \quad (5)$$

[22] Estimates of C_3 can be obtained by fitting the analytical solution in equation (3) to the observed SST and SSS sections across the Latex10 front. The strain rate γ can be computed from the dispersion patterns of the Lyap01 and Lyap02 Lagrangian drifter arrays. Since the CTD profiles collected during Latex10 evidenced a mixed layer depth of about 20 m (see supporting information), we can combine the two through equation (5) to obtain values of submesoscale eddy diffusivity within the upper mixed layer from in situ observations.

3. Results

3.1. Characteristics of the Front

[23] A sequence of successive maps of pseudo-SST from 8 to 15 September is shown in Figure 2. Available drifter trajectories within 1.5 days before and 1.5 days after the date of each image are also superimposed on the pseudo-SST maps. The three drifters deployed before 8 September (indicated by squares in Figure 2) were tethered to 50 m drogues. The nine drifters launched over the western part of the GoL continental shelf on 12 September (indicated by circles in Figure 2) were tethered to 15 m drogues. They correspond to the Lyap01 drifter array deployment.

[24] The temporal evolution of the pseudo-SST maps evidences that, starting from 8 September, warmer waters originally in the eastern part of the GoL were advected westward along the continental slope. The three drifter trajectories along the continental slope show an analogous pattern, suggesting that the westward advection was not limited to the surface layer but extended down to at least 50 m depth. The trajectories of the Lyap01 drifters indicate that over the same period, in the western part of the GoL, colder waters from the continental shelf were advected southward, out of the GoL. The convergence between the warmer waters from the eastern GoL and the colder waters from the western part of the continental shelf (Figure 2, bottom) led to the formation of the front observed during Latex10 (Figure 1, bottom right).

[25] While the southward outflow out of the western part of the GoL can be assumed to be actively generated by wind-induced Ekman transport [e.g., *Petrenko et al.*, 2008; *Hu et al.*, 2011b], the westward advection of eastern-GoL waters along the continental slope is most likely associated with the presence of the Northern Current (hereafter NC). The NC is a strong, mostly geostrophic current which flows

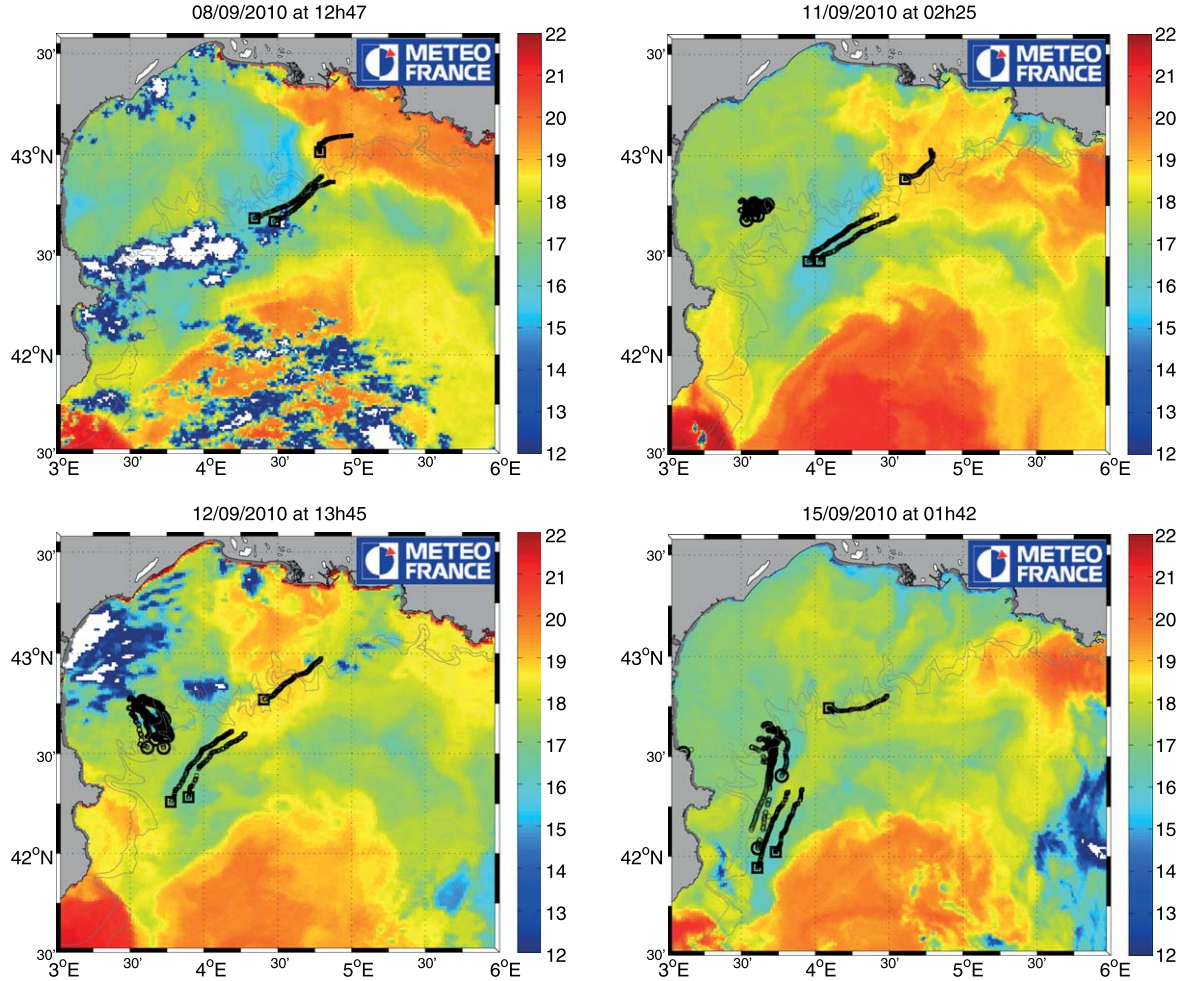


Figure 2. Successive maps of pseudo-SST. Superimposed in black are the drifter positions within 36 h before and after each image was taken (reported on top of each plot). The buoys with 50 m drogues are indicated by squares, whereas the ones with 15 m drogues are indicated by circles. The larger squares/circles indicate the final positions of each drifter. A fourth 50 m drogue drifter was deployed in the eastern GoL before 8 September. However, it quickly stranded ashore and, thus, is not shown.

from east to west along the continental slope, and represents the prominent feature of the GoL's circulation [Millot, 1990]. It is usually characterized by a deep core (>200 m depth), with currents up to 70 cm s^{-1} and a width of ~ 25 km. However, it becomes broader, shallower and less intense during the summer [Petrenko, 2003]. These characteristics are compatible with the westward advection in the upper 50 m observed from pseudo-SST maps and drifter trajectories. Thus, the formation of the Latex10 front in the western GoL was mainly driven by the stirring induced by a combination of wind-induced and large-scale circulation (i.e., the NC), the latter already identified by several studies as one of the main forcings for the development of submesoscale dynamics [e.g., Capet et al., 2008c].

[26] Analysis of the thermohaline characteristics of the front evidences that it was mostly compensated: i.e., the horizontal gradient of temperature was balanced by the salinity gradient, so that the resulting cross-front density profile was almost constant (see the T-S plot in Figure 3, right). This type of fronts is commonly observed at horizontal scales below 10 km [e.g., Rudnick and Ferrari,

1999; Rudnick and Martin, 2002]. With small horizontal variation of density, we expect secondary ageostrophic circulations driven by horizontal gradients of buoyancy to be weak [e.g., Thomas and Lee, 2005]. Therefore, we can assume the dynamics associated with the front to be dominantly horizontal. The effect of the large-scale straining is to induce the stretching of the front along approximately the north-south direction and, at the same time, a thinning of its width along approximately the east-west direction. In the absence of sharp, small-scale variations in surface exchanges of heat and freshwater with the atmosphere, the front width will decrease until the effect of the large-scale straining will be balanced by small-scale turbulent mixing [Ferrari and Polzin, 2005]. Under these assumptions, we can therefore use the front widths of the observed SST and SSS sections to retrieve estimates of small-scale eddy diffusivity.

3.2. Estimates of Front Coefficients

[27] The first step of the analysis was to identify the recorded cross-front sections from the time series of SST

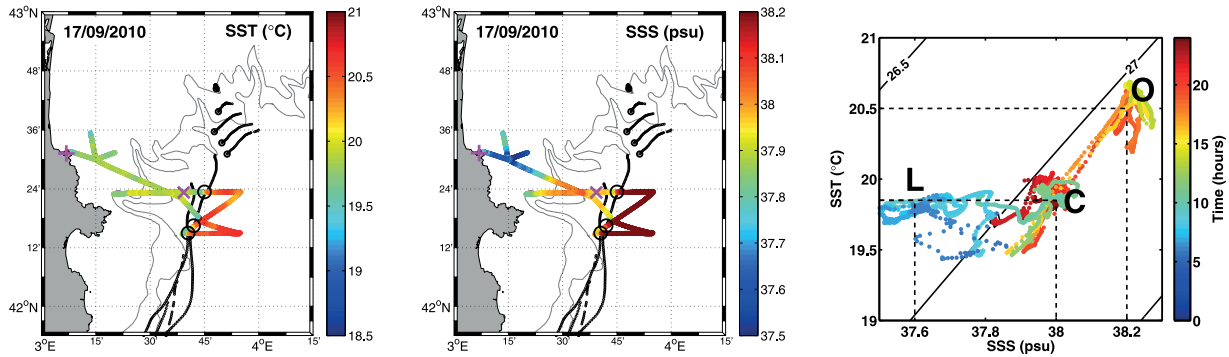


Figure 3. (left) Sea surface temperature recorded by the ship thermosalinograph on 17 September 2010. The beginning and ending point of the ship track are indicated by the + and the x in magenta, respectively. The black circles mark the position of the cross-front sections detected in Figure 4: the southernmost corresponds to section 9, the middle one to 10 and the northernmost to 11. The drifter positions within 24 h before and after 17 September are shown in black as in Figure 2. The five drifters north of 42°30'N corresponds to the Lyap02 array (Figure 7), deployed on 18 September. (middle) Same as the left plot but for sea surface salinity. (right) TS diagram for the surface data from the two maps. Each measurement is color coded according to the time of the day it was collected. The dotted lines indicate the temperature and salinity values associated with the littoral (L), the continental-shelf (C), and the open NW Mediterranean (O) waters. These values were used to identify the cross-front sections (see Figure 4).

and SSS. Here we show the data from 17 September (Figure 3) as an example to illustrate the concepts at the base of the analysis. The same procedure is also applied to the rest of the data collected by the *R/V Le Téthys II* during the Latex10 campaign.

[28] The T-S diagram in Figure 3 evidences that three masses of water marked by distinct T-S signatures were present in the western GoL on 17 September. Littoral waters, observed at the beginning of the ship track, were characterized by the lowest temperatures and salinities ($\sim 19.8^\circ\text{C}$ and ~ 37.6 psu; marked with L). Further off-shore, waters remained relatively cold, but were sensibly more saline ($\sim 19.8^\circ\text{C}$ and ~ 38 psu; marked with C). Comparison with the T-S values observed during the Lyap01 deployment on 12 September confirms that these values were characteristic of the continental-shelf waters advected southward off the GoL. Further east, the continental-shelf waters were in contact with warmer and more saline waters, with T-S values typical of the open NW Mediterranean ($\sim 20.5^\circ\text{C}$ and ~ 38.2 psu; marked with O). As shown in Figure 3 (left and middle), the Lyap01 drifter trajectories closely followed the transition between these two waters. Since to a first approximation those trajectories followed the attractive LCS, they provide a rough indication of the position the Latex10 front. Furthermore, they indicate that the observed open NW Mediterranean waters originated from the eastern GoL and were westward advected by the NC along the continental slope. This is also confirmed by the T-S values observed during the Lyap02 deployment (not shown), performed across the continental slope.

[29] The T-S signatures of continental-shelf and open NW Mediterranean waters were used to define the thresholds to identify the cross-front sections from the time series of SST and SSS (Figure 4). Analysis of the T-S diagrams from the rest of the campaign indicates that the signatures observed on 17 September remained roughly constant during the first part of the cruise. However, T-S values of both

masses of water experienced a decrease in SST ($\sim 0.5^\circ\text{C}$) and SSS (~ 0.05 psu) after 18 September. Such shift was most likely induced by the strong wind and intense rain conditions in the western GoL between 18 and 19 September. The thresholds used for the identification of the cross-front sections were adjusted accordingly. Each cross-front section identified from the analysis of the SST and SSS time series was further inspected by comparing its along-track position with the front position estimated from the Lyap01 and Lyap02 drifter trajectories. A total of 30 cross-front sections were identified: the first one on 14 September, after the Lyap01 deployment; the last one on 23 September.

[30] Figure 4 (left) shows the occurrence of the three cross-front sections identified on 17 September along the time series of SST and SSS for the same day. These corresponds to sections 9, 10, and 11 of the overall 30 sections identified. All three sections are characterized by minimum values of SST and SSS below the lower thresholds used to identify the cross-front sections. These values occur due to the remnants of a colder and less saline patch of water that was detected between the continental-shelf and the open NW Mediterranean waters on both 14 and 15 September. Such patch is also visible in front of the 50 m depth drifters in the pseudo-SST images (Figure 2). The width of section 10 is much broader than the other two. This is due to the differences in the angle at which the ship track intersected the front axis at each passage. To obtain consistent estimates of the front width, each cross section was therefore projected on the orthogonal direction to the front axis, which was derived from the orientation of the attractive LCS reconstructed by Nencioli et al. [2011] (194.5° from the North, i.e., roughly toward SSW).

[31] For each section, SST and SSS observations were best fitted using the analytical solution of the front profile in equation (3). Temperature and salinity sections were always independently used. As an example, SST and SSS

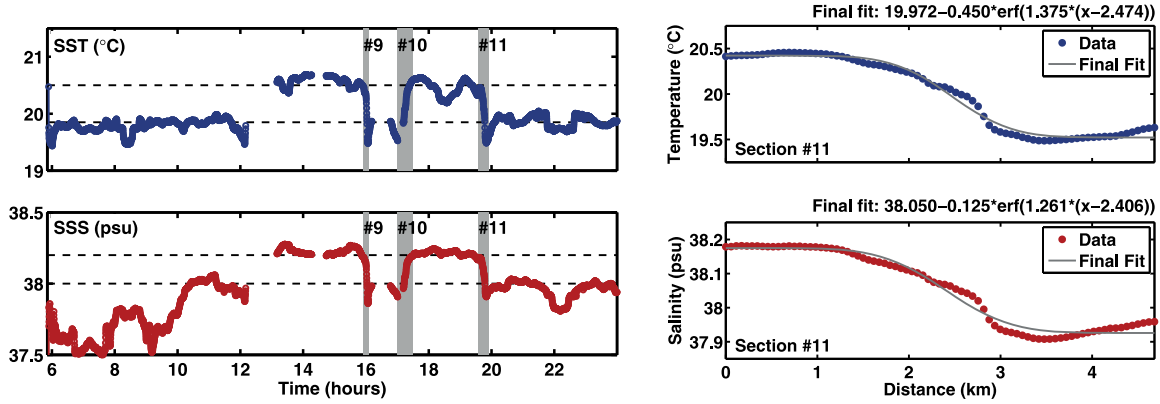


Figure 4. (left) Time series of sea surface temperature (blue) and salinity (red) for 17 September 2010. The dotted lines indicate the values associated with continental-shelf and open NW Mediterranean waters, identified from Figure 3. In gray are evidenced the times of occurrence of three cross-front sections (9, 10, and 11) identified for that day. The gaps in the time series are due to ship operations (i.e., CTD profiling) during which the thermosalinograph was turned off. (right) Across-front temperature (blue) and salinity (red) profiles for section 11. The lines in gray indicate the final fits of the analytical solution of the front profile.

from section 11 are shown in Figure 4 (right). An initial guess for the fit was derived by estimating the values for the coefficients C_1 , C_2 , and C_4 defined in equation (4) from the observations: T_1 was set to the SST or SSS value at the beginning of each section; T_2 to the value at the end of it; and x_0 to half the length of each section. The initial value for the coefficient C_3 was always set to 1, corresponding to the value for the standard error function. Starting from this initial guess, the values of the four coefficients were let vary, and the multivariate best fit was found by applying a Nelder-Mead simplex direct search algorithm [Lagarias *et al.*, 1998] based on a least square estimate. Deriving the initial guess directly from the data allowed to start each least square minimization already close to its expected local minimum. Usually, this guaranteed the algorithm to rapidly converge toward the set of coefficients associated with the appropriate best fitting curve. However, no convergence to a fit for either SST or SSS profiles was found for 11 out of the 30 identified cross-front sections. We interpret that as an indication that our initial assumptions did not hold for those sections, and thus horizontal stirring and small-scale mixing were not the only two processes regulating the front profile (e.g., surface exchanges with the atmosphere and/or frontal instabilities, such as mixed layer eddies [Fox Kemper *et al.*, 2008], ageostrophic anticyclonic instabilities [McWilliams *et al.*, 2004], symmetric instabilities [Taylor and Ferrari, 2009], centrifugal/barotropic instabilities [Munk *et al.*, 2000], were relevant processes, as well). Those sections were discarded from the remainder of the analysis.

[32] Values of C_3 were obtained from each of the SST and SSS sections for which a fit was found, for a total of 38 estimates. As shown in Figure 4 (right) for section 11, the fitted profile usually matched well with the measurements. The observed small deviations can be interpreted as partly due to noise in the measurements, and partly due to mixing processes occurring at scales smaller than the front width. Indeed, it is the contribution of such processes to horizontal

mixing that the estimates of eddy diffusivity at the base of this study aim to parametrize.

[33] The analytical profiles for the 19 cross-front sections of SST and SSS which admitted a fit are shown in Figure 5 (top left and top right, respectively). All profiles were scaled for the coefficients C_1 and C_4 , in order to have them centered on the axis origin. Profiles for which $T_1 > T_2$ (which occurred when the ship track crossed the front from east to west) were also flipped with respect to the y axis. Most of the temperature differences across the front range between 0.5 and 1.0°C, while salinity differences range between 0.2 and 0.3 psu. This is not surprising given the T-S values which characterized the continental shelf and the open NW Mediterranean waters. At the same time, it indirectly confirms that the analytical curves fitted well the observations, since their final SST and SSS limits (T_1 and T_2) depend on the estimated values of the coefficients C_1 and C_2 . The larger SST differences above 1°C correspond to the cross-front sections collected on 14 and 15 September, when (as already mentioned) a colder and less saline mass of water was observed between the continental-shelf and the open NW Mediterranean waters.

[34] Figure 5 (bottom) shows the density (σ_T) profiles obtained from the reconstructed SST and SSS profiles. The profiles were scaled by the C_4 coefficient to have them centered along the x axis, and they were flipped with respect to the y axis when $\sigma_{T1} > \sigma_{T2}$. The figure indicates that the front was generally characterized by small cross-frontal density variations, further confirming its compensated nature. Exceptions are represented by the sections collected between 14 and 15 September, characterized by the presence of the colder and less saline mass of water, and by section 16 collected on 18 September.

[35] The C_3 coefficients from each SST and SSS profile are shown in Figure 6. No consistent trends in the value of C_3 can be observed between noncompensated and compensated profiles, as well as between before and after the storm event between 18 and 19 September. Furthermore, the

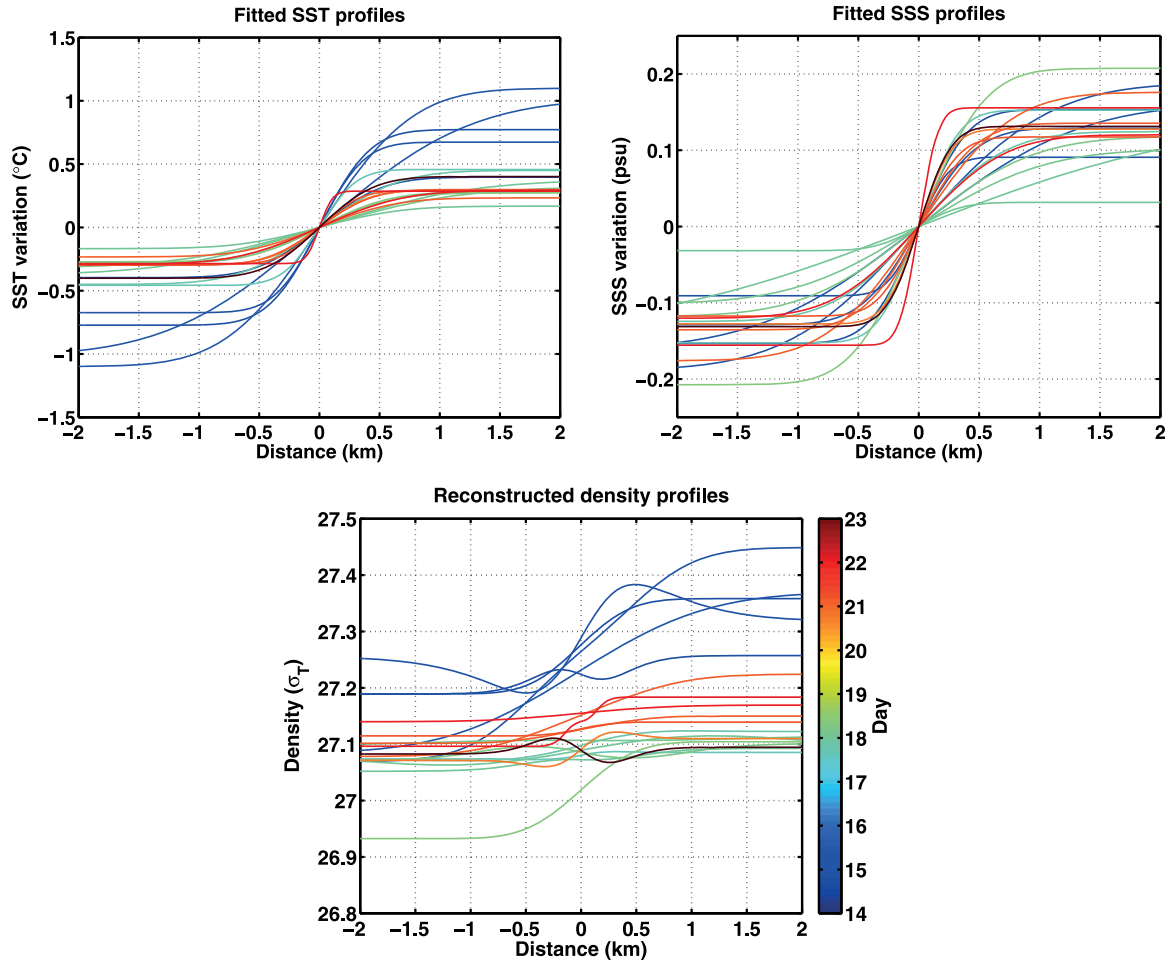


Figure 5. (top) The 19 fitted profiles of (left) SST and (right) SSS collected during the Latex10 campaign. The profiles were shifted along the x and y axes in order to have them centered on the axes origin. (bottom) Density profiles reconstructed from the fitted profiles of SST and SSS. The profiles were shifted along the x axis in order to have them centered on the axis origin. In all three plots, the profiles are color coded according to the day they were collected.

figure indicates that, for each section, values of C_3 from SST are in most cases similar to the values from SSS, although the two tracers are characterized by different ranges of values.

3.3. Estimates of Strain Rate

[36] Values of the strain rate γ were computed from the drifter trajectories of the Lyap01 and Lyap02 deployments (Figure 7, left and middle, respectively). The Lyap01 array included nine drifters which were deployed over the western GoL continental shelf on 12 September. The Lyap02 array included five drifters, deployed across the continental slope on 18 September. The deployment distance between drifters ranged between 3 and 5 km [Nencioli et al., 2011]. Estimates of γ were obtained by computing values of the Lyapunov exponent (hereafter LE). The LE measures the separation rate of trajectories of initially close particles. Lagrangian studies often employ LE computed over a large number of drifter pairs and for different scales of separation to reconstruct LE spectra. These can be analyzed to quantify average dispersion processes, as well as to statistically characterize the regimes at different spatial scales over

dynamically heterogeneous ocean regions [e.g., Lumpkin and Elipot, 2010; Haza et al., 2010; Schroeder et al., 2011, 2012].

[37] In this study, however, we make use of the LE to quantify the rate of stretching of a water parcel induced by a specific dynamical structure over a specific range of

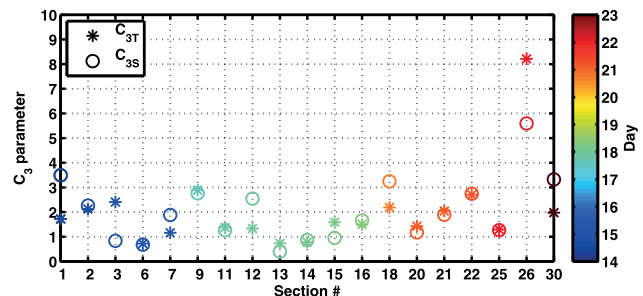


Figure 6. Values of the C_3 parameter from equation (3) estimated from each fitted profile of SST (stars) and SSS (circles) from Figure 5. As in Figure 5, the values are color coded according to the day each profile was collected.

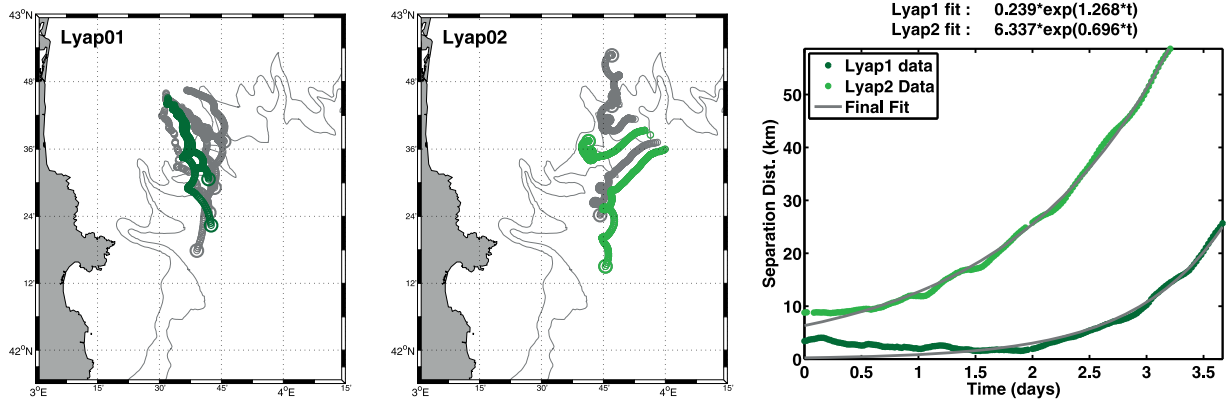


Figure 7. Three day drifter trajectories after the (left) Lyap01 and (middle) Lyap02 array deployments. In each plot, the trajectories in color indicate the drifter couples used to compute the LE $\tilde{\gamma}$. The trajectories of the other deployed drifters are in gray. Only 6 of the 9 Lyap01 drifters are shown in the right plot for figure clarity. (right) Temporal evolution of the separation distance between the fastest separating drifter couples. In gray are the best fitted exponential curves based on equation (6).

spatial scales. The dynamical structure investigated in this study is the velocity field associated with the hyperbolic point defined by the intersection of the attractive and repulsive LCSs identified by *Nencioli et al.* [2011]. The scales of interest are within the mesoscale range, from few to tens of km in the region of study. As evidenced in section 3.1, processes at those scales are the main drivers of the frontal straining. On the other hand, effects of turbulent processes at smaller scales will directly contribute to the estimated eddy diffusivities.

[38] Recent studies have evidenced that spatial scales up to $\mathcal{O}(1-10)$ km can sometimes be characterized by local dispersion regimes [e.g., *Schroeder et al.*, 2012]. However, under intense mesoscale stirring conditions those scales usually show nonlocal dispersion [e.g., *Poje et al.*, 2010; *Schroeder et al.*, 2011]. For this reason, we assumed the dispersion regime at scales of $\mathcal{O}(1-10)$ km associated with the observed LCSs to be nonlocal and, thus, particle separation to be mostly exponential. Under such assumption, the LE is a reliable diagnostic to quantify the integrated local strain rate encountered along a parcel trajectory [e.g., *Waugh and Abraham*, 2008].

[39] To obtain estimates of the LE, we followed a procedure analogous to that used to compute the Finite Size Lyapunov Exponents (FSLE) from the trajectories of synthetic particle clusters [d’Ovidio et al., 2004]. As in the FSLE analysis, the LE was derived from the fastest separating buoy couple of the Lyap01 and Lyap02 cluster deployments (trajectories in color in Figure 7). For each couple, the temporal evolution of their separation distance was fitted by the relationship

$$\delta(t) = \delta_0 e^{\tilde{\gamma}t} \quad (6)$$

which describes the exponential increase of the separation distance δ , from an initial separation δ_0 , under a LE $\tilde{\gamma}$ (Figure 7, right). The best fit was found by applying a method analogous to the one used for the cross-front sections. In this case, only two parameters (δ_0 and $\tilde{\gamma}$) were let vary. The initial guesses were again derived by estimating the two

parameters from the data: by definition, δ_0 was set to the separation distance between the two drifters at $t = 0$; on the other hand, $\tilde{\gamma}$ was computed by inverting equation (6), and setting $\delta(t)$ to the separation distance measured at $t = 3$ days after the deployment.

[40] The exponential curves show a good fit with respect to the data for both deployments, further confirming our nonlocal assumption (see also supporting information). The exponential separation lasted for more than 3 days after the deployment and up to separation distances of more than 50 km for the Lyap02 array. The misfits observed within the first 12 h after the deployment for both curves are most likely due to the initial period of adjustment during which the drifter couple gradually realigned its orientation along the direction of the Lyapunov eigenvector corresponding to the leading LE. This period was shorter for the Lyap02 drifters, which were already deployed roughly perpendicularly across a repelling LCS [Nencioli et al., 2011]. The values of $\tilde{\gamma}$ are $\sim 1.25 \text{ day}^{-1}$ for the Lyap01 array, and $\sim 0.70 \text{ day}^{-1}$ for Lyap02 array, respectively. Both estimates are close to the largest values typically observed along the FSLE ridges used to identify LCSs at the mesoscale from satellite altimetry [e.g., *Lehahn et al.*, 2007; *Beron Vera et al.*, 2008; *d’Ovidio et al.*, 2009; *Hernández Carrasco et al.*, 2012]. This indicates that the hyperbolic point from *Nencioli et al.* [2011] was associated with intense stirring during the whole duration of the Latex10 campaign.

3.4. Submesoscale Horizontal Eddy Diffusivity

[41] The 38 estimates of the C_3 coefficient from the 19 SST and SSS profiles (Figure 6, bottom) and the two estimates of $\tilde{\gamma}$ from the Lyap01 and Lyap02 deployments (Figure 7, right) were combined together using equation (5) to compute a total of 76 estimates of eddy diffusivity (K_H). We decided to apply both values of $\tilde{\gamma}$ for the whole duration of the campaign since they represent average local strain rates over the region. This allowed to obtain a broader range of values of K_H , which (at least partially) accounts for the possible variations of the instantaneous

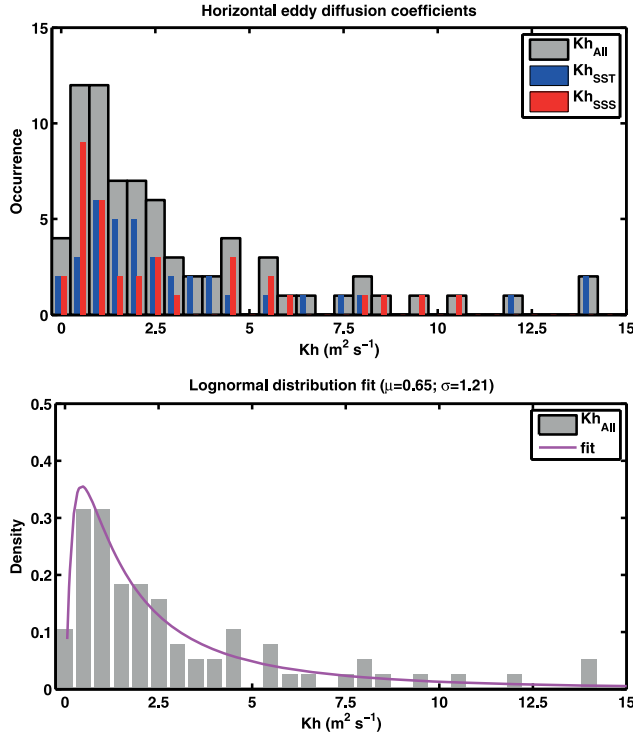


Figure 8. (top) Frequency histogram of the horizontal eddy diffusion coefficients derived by combining the values of the parameter C_3 estimated from the 38 fitted profiles (Figure 6) with the 2 LE $\tilde{\gamma}$ estimated from the drifter deployments (Figure 7). In blue is the distribution of the K_H estimated from the SST profiles; in red the distribution of the K_H from the SSS profiles; and in gray the total distribution of the two combined together. The tail of the distribution includes three further values of K_H larger than $15 \text{ m}^2 \text{ s}^{-1}$ (15.90 , 25.63 , and $46.67 \text{ m}^2 \text{ s}^{-1}$, respectively). (bottom) Density histogram of the horizontal eddy diffusion coefficients superimposed with the fitted log-normal probability density function. The density function is characterized by a location parameter $\mu = 0.65$ and a scale parameter $\sigma = 1.21$.

strain rate experienced by the individual water parcels sampled during different cross sections.

[42] The frequency histogram of the 76 values of K_H is shown in Figure 8 (top). The distribution is markedly skewed to the right (positive skew). It is characterized by a broad peak at values below $2.5 \text{ m}^2 \text{ s}^{-1}$, and by a relatively long tail of episodic occurrences at values above $7.5 \text{ m}^2 \text{ s}^{-1}$. The distribution ranges from a lowest value of $0.06 \text{ m}^2 \text{ s}^{-1}$ to a maximum value of $46.67 \text{ m}^2 \text{ s}^{-1}$.

[43] Despite some expected differences, the distribution of K_H estimated from the SST profiles is characterized by a similar shape as the one from the SSS profiles. This is an important feature, since it evidences that the estimates of K_H using this approach are primarily controlled by the front width (through the C_3 coefficient) and, at the same time, they are relatively independent from the magnitude of the tracer variation ($T_1 - T_2$) across the front. In other words, although being characterized by different ranges of values, SST and SSS profiles from the same section return similar estimates of K_H . This has been already evidenced by the C_3

estimates in Figure 6, and has been further confirmed by scatter plots of K_H versus tracer variation across the front (not shown).

[44] A more robust statistical characterization of our results was obtained by best fitting the distribution of the estimated K_H using various positive skewed analytical distributions. These included Weibull, gamma, chi-square (a special case of gamma), Fréchet, and log-normal distributions. First, the empirical cumulative distribution function (CDF) was constructed from the estimated K_H . Then, the parameters defining the analytical probability density functions (PDF) of the various distributions were obtained by best fitting their respective analytical CDF to the empirical CDF from the data, using the same minimization method used for the cross-front sections and the drifter separation distances. Initial guesses for the parameters were always set to 1. Finally, the goodness of fit of the various distributions was further evaluated by comparing the respective probability-probability (P-P) plots together. In P-P plots, the analytical CDF associated to each value of K_H is plotted against the empirical CDF associated to the same value. Thus, the better the fit, the more the points are aligned along the 1:1 line (see supporting information).

[45] The analysis showed that the observed distribution was best fitted by a log-normal distribution (Figure 8, bottom), implying that the logarithm of K_H is normally distributed. The other distributions all returned worse fits, as they had the tendency of overestimating the occurrence of small values of K_H and/or underestimate the occurrence of higher values (see also supporting information).

[46] Defining the general log-normal PDF as

$$P(x) = \frac{1}{\sigma\sqrt{2\pi}x} e^{-\frac{(\ln x - \mu)^2}{2\sigma^2}}, \quad x > 0 \quad (7)$$

the best fitted PDF was characterized by a location parameter $\mu = 0.65$ and by a scale parameter $\sigma = 1.21$. These two parameters also define all the other statistical properties of the distribution, such as mean ($3.98 \text{ m}^2 \text{ s}^{-1}$), median ($1.92 \text{ m}^2 \text{ s}^{-1}$), and mode ($0.44 \text{ m}^2 \text{ s}^{-1}$), as well as standard deviation ($7.26 \text{ m}^2 \text{ s}^{-1}$) and skewness (11.53). As a log-normal distribution characterizes a variable resulting from the product of many independent positive and identically distributed variables, we can speculate that the observed distribution reflects nonlinear interactions occurring between the different turbulent events parametrized by each estimate of K_H .

[47] The front widths of the observed sections can be computed from the values of the C_3 coefficients. By differentiating equation (3) with respect to x , we can retrieve the equation describing the variation of the tracer gradient across the front. Being the first derivative of the error function, this relation is by definition a Gaussian curve with a width defined by the parameter

$$\sigma = \frac{1}{\sqrt{2}C_3} \quad (8)$$

[48] Thus, we can define the front width as $W = 2\sigma$, which corresponds to the distance, centered at the front axis, within which $\sim 68\%$ of the cross-front tracer variation

occurs [Thorpe, 1983]. Using this definition, we found W ranging from 172 m to 3.5 km, with $\sim 80\%$ of the values between 0.5 and 2 km. The mean front width is ~ 1 km with a standard deviation of ~ 650 m. The front widths range between 1 and 4 km, if a less conservative definition ($W = 4\sigma$, corresponding to $\sim 95\%$ of SST or SSS variation) is adopted.

3.5. Numerical Analysis on the Equilibrium Hypothesis

[49] In section 2.2, the hypothesis of a front at equilibrium made possible to reduce equation (1) to the ordinary differential equation (2) and, thus, to find an analytical expression for the front profile in terms of an error function dependent on constant K_H and γ (equation (3)). As no processes or structures in the oceans can truly reach a steady state, the validity of such hypothesis is always relative to the scales of interest. In our case, we define the front to be at the equilibrium when the time of adjustment from its initial formation has been long enough that its profile approaches the one expected at the idealized steady state under the average large-scale strain rate and local turbulent fluxes. Following such definition, the equilibrium can be considered a “near steady state” at which: (i) the front profile can be approximated by equation (3), and (ii) the highly variable turbulent fluxes still induce adjustments to its shape, although they occur faster and at smaller scales than the initial adjustment.

[50] The analysis of successive cross-front sections following the same water parcel in a Lagrangian reference frame would have provided the most direct way to test the equilibrium hypothesis. Unfortunately, due to constraints in the sampling design, during Latex10 it was not possible to collect such type of observations. Therefore, from our in situ data alone, we could not determine the accuracy of the hypothesis. Instead, the problem was addressed by performing a series of numerical tests based on the advection-diffusion equation (1) in order to investigate the time scales required to reach the idealized steady state given various combinations of constant γ and K_H within the range of the observed values. The equation was discretized in time and space using an explicit method combined with an upwind advection scheme. Using different values (still within our observations range) for the tracer variation across the front, and starting from different initial front profiles (i.e., step-like; linearly increasing), the tests showed that equilibrium was reached relatively fast, with an exponential growth/decay of the front width toward the idealized steady state value within 1–2 days (Figure 9).

[51] Given the horizontal velocities observed in the region, this time interval corresponds to a distance from the hyperbolic point (where the two different water masses originating the front initially converged) on the order of the ones at which the sections were collected. Although this cannot guarantee that all observed sections were at the equilibrium, it confirms that such hypothesis can be at least reasonably assumed. Thus, the width of each observed section can be considered directly related to the history of the local turbulent fluxes, and their integrated effects ultimately parametrized by the estimated K_H . Given the highly variable nature of turbulent processes, this explains, at least partially, the large variability in the observed values of K_H .

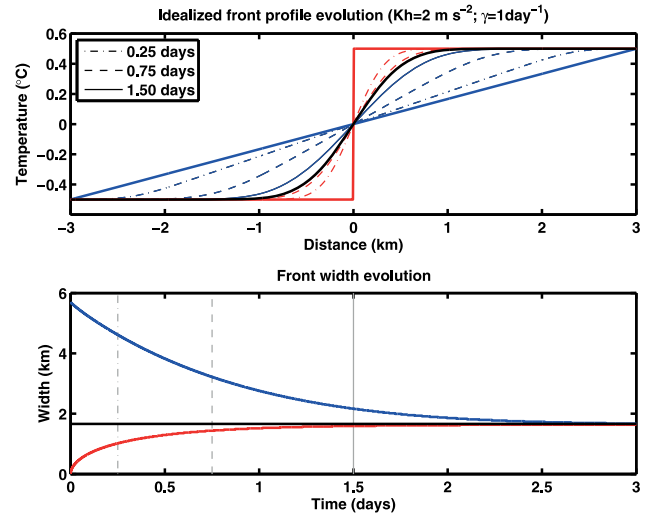


Figure 9. (top) Example of numerical temporal evolution of two idealized temperature fronts (linear gradient in blue; step-like in red) toward the analytical equilibrium profile (black) for a given combination of strain rate (γ) and eddy diffusivity (K_H). The numerical simulations were based on equation (1) using constant values of γ and K_H . The thinner lines mark intermediate front profiles at different times before the equilibrium. The red curve at 1.5 days coincides already with the analytical equilibrium profile (as shown in the bottom plot). (bottom) Temporal evolution of the widths of the linear gradient (blue) and step-like (red) fronts toward the width at the equilibrium (black). The width at the equilibrium was computed as $W = 4\sigma$. The gray lines mark the times corresponding to each intermediate profile plotted in the top plot. The figure indicates a relatively rapid adjustment (on the order of 1–2 days) of the front profile toward the equilibrium. Analogous results were obtained for various combinations of K_H and γ within the range of the observed values.

At the same time, as our estimates of K_H are quadratically dependent on the width-coefficients C_3 , errors introduced by front widths estimated at uncertain equilibrium conditions could also have contributed to such variability.

4. Discussion and Conclusions

[52] In this study, we have presented an approach to estimate eddy diffusivity coefficients K_H from in situ observations across a front in the western part of the GoL during the Latex10 campaign (September 2010). The method is based on the hypothesis that the shape of the front profile at the equilibrium results from a balance between the strain induced by large-scale dynamics and the local small-scale mixing. Under such assumption, an analytical expression for the front profile can be found in terms of an error function scaled by four coefficients. The analytical profile was fitted to a series of SST and SSS sections collected across the front. The coefficient defining the width of the fitted curve depends exclusively on the cross-front eddy diffusivity K_H and the strain rate γ . Values of γ were quantified by computing the LE $\tilde{\gamma}$ from the analysis of the exponential separation of Lagrangian drifter couples from two

successive drifter array deployments (1.25 day^{-1} and 0.70 day^{-1} , respectively). By combining the width coefficients from the fitted profiles with the concomitant estimates of the LE, it was possible to retrieve a total of 76 estimates of K_H .

[53] The resulting frequency histogram of K_H is characterized by a marked positive skew. Among various analytical positive skewed distribution, a log-normal distribution with location parameter $\mu = 0.65$ and scale parameter $\sigma = 1.21$ was identified as the best fit to the observed distribution. Such distribution is characterized by mean, median and mode values of K_H of $3.98 \text{ m}^2 \text{ s}^{-1}$, $1.92 \text{ m}^2 \text{ s}^{-1}$, and $0.44 \text{ m}^2 \text{ s}^{-1}$, respectively. Overall we have found that 70% of the values of K_H range between 0.4 and $5 \text{ m}^2 \text{ s}^{-1}$. This is in agreement with the estimates from passive-tracer experiments by *Ledwell et al.* [1998] and *Abraham et al.* [2000], who obtained a K_H of 2 and $4 \text{ m}^2 \text{ s}^{-1}$, respectively, for length-scales of $\mathcal{O}(1\text{--}10)\text{ km}$. On the other hand, our results suggest that values of $\sim 20 \text{ m}^2 \text{ s}^{-1}$ for analogous length-scales found from other passive-tracer experiments by *Stanton et al.* [1998] and *Martin et al.* [2001] might have overestimated K_H .

[54] Our estimates of K_H are associated with front widths between 1 and 4 km . Eddy diffusivity derived in this study parametrizes the horizontal mixing induced by highly variable turbulent processes occurring at scales smaller than these. Therefore, by developing a new approach in which information from drifter trajectories is combined with ship-based in situ measurements, we have been able to obtain estimates of K_H at smaller spatial scales than previous studies based exclusively on Lagrangian observations.

[55] The hypothesis that the observed front profiles were at a near steady state could not be directly tested from the in situ observations. Therefore, we performed a series of numerical tests based on the advection diffusion equation (1), which indicate that such hypothesis can be reasonably assumed.

[56] This study provides an important set of in situ observations for both high resolution, as well as MOLES models. Although K_H does not effectively parametrize all subgrid scale processes (e.g., dispersion; upgradient/inverse cascade), our estimates represent a significant contribution for evaluating and eventually improving model performances. They represent a useful benchmark for setting-up and tuning the eddy diffusivity coefficients in high-resolution numerical simulations capable of resolving frontal structures with spatial scales similar to the ones observed. On the other hand, they can be directly used as model parametrization in MOLES (as well as low-resolution) models and can provide a term of reference for further testing and refining the different closure schemes adopted. The proposed method for deriving K_H from measurements of front profiles and the associated strain rates could also become a valid approach for evaluating the total diffusivity (physical as well as numerical) associated with specific high-resolution model setups. At the same time, applying the method to high-resolution simulations will help to better assess the robustness of some of the assumptions at the base of our approach (e.g., the equilibrium hypothesis).

[57] The approach presented in this study represents a valid alternative to passive-tracer experiments for obtaining in situ estimates of small-scale eddy diffusivity, since it

presents some important advantages: most notably, reduced costs (being based exclusively on ship-based thermosalinograph measurements and Lagrangian drifter trajectories), and easier implementation (for instance, not requiring ship-based Lagrangian operations for the release, as well as the successive mapping of the passive-tracer patch). The main difficulty of the method consists on the initial identification, and the successive sampling of the frontal structure. In fact, despite recent technological advancements, adequate sampling of submesoscale structures remains an observational challenge due to their ephemeral and localized nature [e.g., *Lévy et al.*, 2012]. Therefore, it is essential that future dedicated field experiments will be based on adaptive campaigns during which the sampling strategy will be routinely adjusted based on near-real time analysis of the available in situ as well as remote sensed observations [e.g., *Nencioli et al.*, 2011].

[58] Future campaigns specifically designed around the approach presented in this study will be required to further refine our estimates of K_H . In particular, while a large variability in the observed K_H is expected due to the nature of turbulent processes, uncertainties on the equilibrium state of the front for each observed section also played a role. A sampling strategy (e.g., Lagrangian sampling) designed to directly assess the front state could reduce such contribution by providing more accurate equilibrium widths and, hence, more accurate estimates of K_H .

[59] Further in situ estimates will also allow to investigate the spatial and temporal variability of K_H , and thus test its isotropy at the small-scales. The analysis should not be limited to the horizontal only, but also extended to the vertical. High resolution vertical sections from recently developed profiling platforms (e.g., gliders; ship-towed profilers), combined with drifters tethered with drogues at different depths, can provide estimates of K_H throughout the whole upper water column. At the same time, the vertical sections can be also used for better characterizing the baroclinic/barotropic nature of the observed structures. On the one hand, this will allow a greater generalization of the results. On the other, it will allow the direct investigation of the role of frontal strain in suppressing frontal instabilities [e.g., *Bishop*, 1993; *Spall*, 1997; *McWilliams et al.*, 2009], for instance, by comparing the estimated eddy diffusivities with the ones parametrized by *Fox Kemper et al.* [2008].

[60] Finally, being based on the analysis of front width and strain rate, the approach is not limited to in situ observations only, but can also be applied to remote sensed measurements. Currently, remote sensed SST can already provide surface fields at the km scale, whereas, altimetry derived velocities are still relatively coarse. At the same time, Lagrangian diagnostics such as the LE can extract information at smaller scales than the resolution of the velocity field [*d'Ovidio et al.*, 2004]. Furthermore, future satellite missions based on new generation altimeters (e.g., Surface Water and Ocean Topography, SWOT) [*Fu and Ferrari*, 2008] will allow to retrieve surface velocity fields at even higher resolutions. For these reasons, our approach could open important perspectives for the development of remote sensed global analyses of the spatial and temporal variability of submesoscale eddy diffusivity.

[61] **Acknowledgments.** This work is a contribution to the SWOT Science Definition Team. The LATEX project was supported by the programs LEFE/IDAO and LEFE/CYBER of the INSU-Institut National des Sciences de l'Univers and by the Region PACA-Provence Alpes Côte d'Azur. F.N. acknowledges support from the FP7 Marie Curie Actions of the European Commission, via the Intra-European Fellowship (FP7-PEOPLE-IEF-2011), project "Lyapunov Analysis in the COASTal Environment" (LACOSTE-299834). AVHRR data were supplied by Météo-France. The DT-INSU is thanked for the treatment of the thermosalinograph data. The authors thank the three anonymous reviewers, whose comments and suggestions greatly improved the quality of this work.

References

- Abernathy, R. P., and J. Marshall (2013), Global surface eddy diffusivities derived from satellite altimetry, *J. Geophys. Res.*, **118**, 901–916, doi:10.1002/jgrc.20066.
- Abraham, E. R., C. S. Law, P. W. Boyd, S. J. Lavender, M. T. Maldonado, and A. R. Bowie (2000), Importance of stirring in the development of an iron-fertilized phytoplankton, *Nature*, **407**(6805), 727–730.
- Beron Vera, F. J., M. J. Olascoaga, and G. J. Goni (2008), Oceanic mesoscale eddies as revealed by Lagrangian coherent structures, *Geophys. Res. Lett.*, **35**, L12603, doi:10.1029/2008GL033957.
- Bishop, C. H. (1993), On the behaviour of baroclinic waves undergoing horizontal deformation. II: Error-blund amplification and Rossby wave diagnostics, *Q. J. R. Meteorol. Soc.*, **119**(510), 241–267, doi:10.1002/qj.49711951003.
- Boccaletti, G., R. Ferrari, and B. Fox Kemper (2007), Mixed layer instabilities and restratification, *J. Phys. Oceanogr.*, **37**(9), 2228–2250.
- Bracco, A., S. Clayton, and C. Pasquero (2009), Horizontal advection, diffusion, and plankton spectra at the sea surface, *J. Geophys. Res.*, **114**, C02001, doi:10.1029/2007JC004671.
- Calil, P. H. R., and K. J. Richards (2010), Transient upwelling hot spots in the oligotrophic North Pacific, *J. Geophys. Res.*, **115**, C02003, doi:10.1029/2009JC005360.
- Campbell, R., F. Diaz, Z. Hu, A. Doglioli, A. Petrenko, and I. Dekeyser (2012), Nutrients and plankton spatial distributions induced by a coastal eddy in the Gulf of Lion: Insights from a numerical model, *Prog. Oceanogr.*, **109**, 47–69, doi:10.1016/j.pocan.2012.09.005.
- Capet, X., J. C. McWilliams, M. J. Molemaker, and A. F. Shchepetkin (2008a), Mesoscale to submesoscale transition in the California current system. Part III: Energy balance and flux, *J. Phys. Oceanogr.*, **38**(10), 2256–2269.
- Capet, X., J. C. McWilliams, M. J. Molemaker, and A. F. Shchepetkin (2008b), Mesoscale to submesoscale transition in the California current system. Part I: Flow structure, eddy flux, and observational tests, *J. Phys. Oceanogr.*, **38**(1), 29–43.
- Capet, X., J. C. McWilliams, M. J. Molemaker, and A. F. Shchepetkin (2008c), Mesoscale to submesoscale transition in the California current system. Part II: Frontal Processes, *J. Phys. Oceanogr.*, **38**(1), 44–64.
- d'Ovidio, F., V. Fernández, E. Hernández García, and C. López (2004), Mixing structures in the Mediterranean Sea from finite-size Lyapunov exponents, *Geophys. Res. Lett.*, **31**, L17203, doi:10.1029/2004GL020328.
- d'Ovidio, F., J. Isern Fontanet, C. López, E. Hernández García, and E. García Ladona (2009), Comparison between Eulerian diagnostics and finite-size Lyapunov exponents computed from altimetry in the Algerian basin, *Deep Sea Res., Part I*, **56**(1), 15–31, doi:10.1016/j.dsr.2008.07.014.
- Ferrari, R., and K. L. Polzin (2005), Finescale structure of the T-S relation in the Eastern North Atlantic, *J. Phys. Oceanogr.*, **35**(8), 1437–1454.
- Flament, P., L. Armi, and L. Washburn (1985), The evolving structure of an upwelling filament, *J. Geophys. Res.*, **90**(C6), 11,765–11,778.
- Fox Kemper, B., and D. Menemenlis (2008), *Can Large Eddy Simulation Techniques Improve Mesoscale Rich Ocean Models?*, pp. 319–337, AGU, Washington, D. C., doi:10.1029/177GM19.
- Fox Kemper, B., R. Ferrari, and R. Hallberg (2008), Parameterization of mixed layer eddies. Part I: Theory and diagnosis, *J. Phys. Oceanogr.*, **38**(6), 1145–1165.
- Fu, L.-L., and R. Ferrari (2008), Observing oceanic submesoscale processes from space, *Eos Trans. AGU*, **89**(48), 488.
- Gower, J. F. R., K. L. Denman, and R. J. Holyer (1980), Phytoplankton patchiness indicates the fluctuation spectrum of mesoscale oceanic structure, *Nature*, **288**(5787), 157–159.
- Griffa, A., K. Owens, L. Piterbarg, and B. Rozovskii (1995), Estimates of turbulence parameters from Lagrangian data using a stochastic particle model, *J. Mar. Res.*, **53**(3), 371–401, doi:10.1357/0022240953213151.
- Haza, A. C., T. M. Özgökmen, A. Griffa, A. Molcard, P.-M. Poulain, and G. Peglion (2010), Transport properties in small-scale coastal flows: Relative dispersion from VHF radar measurements in the Gulf of La Spezia, *Ocean Dyn.*, **60**(4), 861–882, doi:10.1007/s10236-010-0301-7.
- Hernández Carrasco, I., C. López, E. Hernández García, and A. Turiel (2012), Seasonal and regional characterization of horizontal stirring in the global ocean, *J. Geophys. Res.*, **117**, C10007, doi:10.1029/2012JC008222.
- Hu, Z., A. Petrenko, A. Doglioli, and I. Dekeyser (2011a), Study of a mesoscale anticyclonic eddy in the western part of the Gulf of Lion, *J. Mar. Syst.*, **88**(1), 3–11, doi:10.1016/j.jmarsys.2011.02.008.
- Hu, Z. Y., A. A. Doglioli, A. M. Petrenko, P. Marsaleix, and I. Dekeyser (2009), Numerical simulations of eddies in the Gulf of Lion, *Ocean Modell.*, **28**(4), 203–208, doi:10.1016/j.ocemod.2009.02.004.
- Hu, Z. Y., A. A. Petrenko, A. M. Doglioli, and I. Dekeyser (2011b), Numerical study of eddy generation in the western part of the Gulf of Lion, *J. Geophys. Res.*, **116**, C12030, doi:10.1029/2011JC007074.
- James, I. (1996), Advection schemes for shelf sea models, *J. Mar. Syst.*, **8**(34), 237–254, doi:10.1016/0924-7963(96)00008-5.
- Kersalé, M., A. A. Petrenko, A. M. Doglioli, I. Dekeyser, and F. Nencioli (2013), Physical characteristics and dynamics of the coastal Latex09 Eddy derived from in situ data and numerical modeling, *J. Geophys. Res.*, **118**, 399–409, doi:10.1029/2012JC008229.
- Klein, P., B. L. Hua, G. Lapeyre, X. Capet, S. Le Gentil, and H. Sasaki (2008), Upper ocean turbulence from high-resolution 3D simulations, *J. Phys. Oceanogr.*, **38**(8), 1748–1763.
- Klocker, A., R. Ferrari, J. H. Lacasce, and S. T. Merrifield (2012), Reconciling float-based and tracer-based estimates of lateral diffusivities, *J. Mar. Res.*, **70**(4), 569–602.
- LaCasce, J. (2008), Statistics from Lagrangian observations, *Prog. Oceanogr.*, **77**(1), 1–29, doi:10.1016/j.pocan.2008.02.002.
- Lagarias, J., J. Reeds, M. Wright, and P. Wright (1998), Convergence properties of the Nelder-Mead simplex method in low dimensions, *SIAM J. Optim.*, **9**(1), 112–147, doi:10.1137/S1052623496303470.
- Le Sommer, J., F. d'Ovidio, and G. Madec (2011), Parameterization of sub-grid stirring in eddy resolving ocean models. Part 1: Theory and diagnostics, *Ocean Modell.*, **39**(12), 154–169, doi:10.1016/j.ocemod.2011.03.007.
- Ledwell, J. R., A. J. Watson, and C. S. Law (1998), Mixing of a tracer in the pycnocline, *J. Geophys. Res.*, **103**(C10), 21,499–21,529.
- Légaras, B., I. Pissot, G. Berthet, and F. Lefèvre (2005), Variability of the Lagrangian turbulent diffusion in the lower stratosphere, *Atmos. Chem. Phys.*, **5**(6), 1605–1622, doi:10.5194/acp-5-1605-2005.
- Lehahn, Y., F. d'Ovidio, M. Levy, and E. Heifetz (2007), Stirring of the northeast Atlantic spring bloom: A Lagrangian analysis based on multi-satellite data, *J. Geophys. Res.*, **112**(C8), C08005, doi:10.1029/2006JC003927.
- Lévy, M., P. Klein, and A.-M. Treguier (2001), Impact of sub-mesoscale physics on production and subduction of phytoplankton in an oligotrophic regime, *J. Mar. Res.*, **59**(4), 535–565.
- Lévy, M., R. Ferrari, P. J. S. Franks, A. P. Martin, and P. Rivière (2012), Bringing physics to life at the submesoscale, *Geophys. Res. Lett.*, **39**, L14602, doi:10.1029/2012GL052756.
- Lumpkin, R., and S. Elipot (2010), Surface drifter pair spreading in the North Atlantic, *J. Geophys. Res.*, **115**, C12017, doi:10.1029/2010JC006338.
- Lumpkin, R., A.-M. Treguier, and K. Speer (2002), Lagrangian eddy scales in the Northern Atlantic Ocean, *J. Phys. Oceanogr.*, **32**(9), 2425–2440, doi:10.1175/1520-0485(2002)032<2425:LESITN>2.0.CO;2.
- Mahadevan, A., E. D'Asaro, C. Lee, and M. J. Perry (2012), Eddy-driven stratification initiates North Atlantic spring phytoplankton blooms, *Science*, **337**(6090), 54–58, doi:10.1126/science.1218740.
- Marchesiello, P., X. Capet, C. Menkes, and S. C. Kennan (2011), Submesoscale dynamics in tropical instability waves, *Ocean Modell.*, **39**(1–2), 31–46, doi:10.1016/j.ocemod.2011.04.011.
- Marshall, J., E. Shuckburgh, H. Jones, and C. Hill (2006), Estimates and implications of surface eddy diffusivity in the Southern Ocean derived from tracer transport, *J. Phys. Oceanogr.*, **36**(9), 1806–1821.
- Martin, A. P., K. J. Richards, C. S. Law, and M. Liddicoat (2001), Horizontal dispersion within an anticyclonic mesoscale eddy, *Deep Sea Res., Part II*, **48**, 739–755, doi:10.1016/S0967-0645(00)00095-3.

- McWilliams, J. C., M. J. Molemaker, and I. Yavneh (2004), Ageostrophic, anticyclonic instability of a geostrophic, barotropic boundary current, *Phys. Fluids*, 16(10), 3720–3725, doi:10.1063/1.1785132.
- McWilliams, J. C., M. J. Molemaker, and E. I. Olafsdottir (2009), Linear fluctuation growth during frontogenesis, *J. Phys. Oceanogr.*, 39(12), 3111–3129, doi:10.1175/2009JPO4186.1.
- Millot, C. (1982), Analysis of upwelling in the Gulf of Lions, in *Hydrodynamics of Semi-Enclosed Seas: Proceedings of the 13th International Liège Colloquium on Ocean Hydrodynamics*, vol. 34, edited by J. C. J. Nihoul, Elsevier Oceanogr. Ser., pp. 143–153, Elsevier, Amsterdam.
- Millot, C. (1990), The Gulf of Lions' hydrodynamics, *Cont. Shelf Res.*, 10, 885–894, doi:10.1016/0278-4343(90)90065-T.
- Molemaker, M. J., J. C. McWilliams, and X. Capet (2010), Balanced and unbalanced routes to dissipation in an equilibrated Eady flow, *J. Fluid Mech.*, 654, 35–63, doi:10.1017/S0022112009993272.
- Munk, W., L. Armi, K. Fischer, and F. Zachariasen (2000), Spirals on the sea, *Proc. R. Soc. London, Ser. A*, 456(1997), 1217–1280, doi:10.1098/rspa.2000.0560.
- Nakamura, N. (1996), Two-dimensional mixing, edge formation, and permeability diagnosed in an area coordinate, *J. Atmos. Sci.*, 53(11), 1524–1537.
- Nakamura, N. (2001), A new look at eddy diffusivity as a mixing diagnostic, *J. Atmos. Sci.*, 58(24), 3685–3701.
- Nencioli, F., F. d'Ovidio, A. M. Doglioli, and A. A. Petrenko (2011), Surface coastal circulation patterns by in-situ detection of Lagrangian coherent structures, *Geophys. Res. Lett.*, 38, L17604, doi:10.1029/2011GL048815.
- Ohlmann, J. C., J. H. LaCasce, L. Washburn, A. J. Mariano, and B. Emery (2012), Relative dispersion observations and trajectory modeling in the Santa Barbara Channel, *J. Geophys. Res.*, 117, C05040, doi:10.1029/2011JC007810.
- Okubo, A. (1971), Oceanic diffusion diagrams, *Deep Sea Res. Oceanogr. Abstr.*, 18(8), 789–802, doi:10.1016/0011-7471(71)90046-5.
- Özgökmen, T. M., T. Iliescu, and P. F. Fischer (2009), Large eddy simulation of stratified mixing in a three-dimensional lock-exchange system, *Ocean Modell.*, 26(3–4), 134–155, doi:10.1016/j.ocemod.2008.09.006.
- Özgökmen, T. M., A. C. Poje, P. F. Fischer, and A. C. Haza (2011), Large eddy simulations of mixed layer instabilities and sampling strategies, *Ocean Modell.*, 39(3–4), 311–331, doi:10.1016/j.ocemod.2011.05.006.
- Perruche, C., P. Rivière, G. Lapeyre, X. Carton, and P. Pondaven (2011), Effects of surface quasi-geostrophic turbulence on phytoplankton competition and coexistence, *J. Mar. Res.*, 69(1), 105–135, doi:10.1357/002224011798147606.
- Petrenko, A. (2003), Variability of circulation features in the gulf of lion NW Mediterranean Sea: Importance of inertial currents, *Oceanol. Acta*, 26(4), 323–338, doi:10.1016/S0399-1784(03)00038-0.
- Petrenko, A. A., C. Dufau, and C. Estournel (2008), Barotropic eastward currents in the western Gulf of Lion, northwestern Mediterranean Sea, during stratified conditions, *J. Mar. Syst.*, 74(1–2), 406–428, doi:10.1016/j.jmarsys.2008.03.004.
- Pisso, I., E. Real, K. S. Law, B. Legras, N. Bousserez, J. L. Atti, and H. Schlager (2009), Estimation of mixing in the troposphere from Lagrangian trace gas reconstructions during long-range pollution plume transport, *J. Geophys. Res.*, 114, D19301, doi:10.1029/2008JD011289.
- Poje, A. C., A. C. Haza, T. M. Özgökmen, M. G. Magaldi, and Z. D. Garraffo (2010), Resolution dependent relative dispersion statistics in a hierarchy of ocean models, *Ocean Modell.*, 31(1–2), 36–50, doi:10.1016/j.ocemod.2009.09.002.
- Ramachandran, S., A. Tandon, and A. Mahadevan (2013), Effect of subgrid-scale mixing on the evolution of forced submesoscale instabilities, *Ocean Modell.*, 66, 45–63, doi:10.1016/j.ocemod.2013.03.001.
- Rudnick, D. L., and R. Ferrari (1999), Compensation of horizontal temperature and salinity gradients in the ocean mixed layer, *Science*, 283(5401), 526–529, doi:10.1126/science.283.5401.526.
- Rudnick, D. L., and J. P. Martin (2002), On the horizontal density ratio in the upper ocean, *Dyn. Atmos. Oceans*, 36(1–3), 3–21, doi:10.1016/S0377-0265(02)00022-2.
- Rypina, I. I., I. Kamenkovich, P. Berloff, and L. J. Pratt (2012), Eddy-induced particle dispersion in the near-surface North Atlantic, *J. Phys. Oceanogr.*, 42(12), 2206–2228.
- Sallée, J., K. Speer, R. Morrow, and R. Lumpkin (2008), An estimate of Lagrangian eddy statistics and diffusion in the mixed layer of the Southern Ocean, *J. Mar. Res.*, 66(4), 441–463.
- Schroeder, K., A. C. Haza, A. Griffa, T. M. Özgökmen, P. M. Poulain, R. Gerin, G. Peggion, and M. Rixen (2011), Relative dispersion in the Liguro-Provençal basin: From sub-mesoscale to mesoscale, *Deep Sea Res., Part I*, 58(3), 209–228, doi:10.1016/j.dsr.2010.11.004.
- Schroeder, K., et al. (2012), Targeted Lagrangian sampling of submesoscale dispersion at a coastal frontal zone, *Geophys. Res. Lett.*, 39, L11608, doi:10.1029/2012GL051879.
- Shuckburgh, E., H. Jones, J. Marshall, and C. Hill (2009), Understanding the regional variability of eddy diffusivity in the Pacific sector of the Southern Ocean, *J. Phys. Oceanogr.*, 39(9), 2011–2023.
- Smagorinsky, J. (1963), General circulation experiments with the primitive equations. I: The basic experiment, *Mon. Weather Rev.*, 91(3), 99–164.
- Spall, M. A. (1997), Baroclinic jets in confluent flow, *J. Phys. Oceanogr.*, 27(6), 1054–1071, doi:10.1175/1520-0485(1997)027<1054:BJICF>2.0.CO;2.
- Stanton, T., C. Law, and A. Watson (1998), Physical evolution of the IronEx-I open ocean tracer patch, *Deep Sea Res., Part II*, 45(6), 947–975, doi:10.1016/S0967-0645(98)00018-6.
- Taylor, J. R., and R. Ferrari (2009), On the equilibration of a symmetrically unstable front via a secondary shear instability, *J. Fluid Mech.*, 622, 103–113, doi:10.1017/S0022112008005272.
- Taylor, J. R., and R. Ferrari (2010), Buoyancy and wind-driven convection at mixed layer density fronts, *J. Phys. Oceanogr.*, 40(6), 1222–1242.
- Thomas, L. N., and C. M. Lee (2005), Intensification of ocean fronts by down-front winds, *J. Phys. Oceanogr.*, 35(6), 1086–1102.
- Thomas, L. N., A. Tandon, and A. Mahadevan (2008), Submesoscale processes and dynamics, in *Ocean Modeling in an Eddying Regime*, *Geophys. Monogr. Ser.*, vol. 177, edited by M. W. Hecht and H. Hasumi, pp. 17–38, AGU, Washington, D. C.
- Thorpe, S. A. (1983), Benthic observations on the Madeira abyssal plain: Fronts, *J. Phys. Oceanogr.*, 13(8), 1430–1440.
- Waugh, D. W., and E. R. Abraham (2008), Stirring in the global surface ocean, *Geophys. Res. Lett.*, 35, L20605, doi:10.1029/2008GL035526.
- Zhurbas, V., and I. S. Oh (2004), Drifter-derived maps of lateral diffusivity in the Pacific and Atlantic Oceans in relation to surface circulation patterns, *J. Geophys. Res.*, 109, C05015, doi:10.1029/2003JC002241.